True S-cones are concentrated in the ventral mouse retina and wired for color detection in the upper visual field

Francisco M. Nadal-Nicolás[1],*, Vincent P. Kunze[1],†, John M. Ball[1],†, Brian T. Peng[1],†, Akshay Krisnan[1],†, Gaohui Zhou[1],†, Lijin Dong[2], Wei Li[1],*.

[1]*Retinal Neurophysiology Section, National Eye Institute, National Institutes of Health, Bethesda, Maryland, USA.*
[2]*Genetic Engineering Facility, National Eye Institute, National Institutes of Health, Bethesda, Maryland, USA.*

†Equal contribution
*Corresponding authors

ABSTRACT

Color, an important visual cue for survival, is encoded by comparing signals from photoreceptors with different spectral sensitivities. The mouse retina expresses a short wavelength-sensitive and a middle/long wavelength-sensitive opsin (S- and M-opsin), forming opposing, overlapping gradients along the dorsal-ventral axis. Here, we analyzed the distribution of all cone types across the entire retina for two commonly used mouse strains. We found, unexpectedly, that "true S-cones" (S-opsin only) are highly concentrated (up to 30% of cones) in ventral retina. Moreover, S-cone bipolar cells (SCBCs) are also skewed towards ventral retina, with wiring patterns matching the distribution of true S-cones. In addition, true S-cones in the ventral retina form clusters, which may augment synaptic input to SCBCs. Such a unique true S-cone and SCBC connecting pattern forms a basis for mouse color vision, likely reflecting evolutionary adaption to enhance color coding for the upper visual field suitable for mice's habitat and behavior.

KEYWORDS

Genuine S-cone, cone distribution, cone cluster, mammalian photoreceptor, S-cone bipolar cells, blue bipolar cells, color vision.

1. INTRODUCTION

Topographic representation of the visual world in the brain originates from the light-sensitive photoreceptors in the retina (Rhim et al., 2017). Although the neuronal architecture of the retina is similar among different vertebrates, the numbers and distributions of photoreceptors vary considerably (Hunt and Peichl, 2014). Such patterns have been evolutionarily selected, adapting to the animal's unique behavior (diurnal or nocturnal) and lifestyle (prey or predator) for better use of the visual information in the natural environment (Dominy and Lucas, 2001; Gerl and Morris, 2008; Peichl, 2005). Color, an important visual cue for survival, is encoded by comparing signals carried by photoreceptors with different spectral preferences (Baden and Osorio, 2019). While amongst mammals, trichromatic color vision is privileged for some primates (Jacobs et al., 1996; Nathans et al., 1986; Yokoyama and Yokoyama, 1989), most terrestrial mammals are dichromatic (Marshak and Mills, 2014; Puller and Haverkamp, 2011; Jacobs, 1993). The mouse retina expresses two types of cone opsins, S- and M-opsin, with peak sensitivities at 360 nm and 508 nm, respectively (Jacobs et al., 1991; Nikonov et al., 2006). The expression patterns of these two opsins form opposing and overlapping gradients along the dorsal-ventral axis, resulting in a majority of cones expressing both opsins (herein either "mixed cones" or M^+S^+) (Applebury et al., 2000; Ng et al., 2001; Wang et al., 2011). Thus, S-opsin enrichment in the ventral retina better detects short-wavelength light from the sky, and M-opsin in the dorsal retina perceives the ground (e.g., a grassy field) (Baden et al., 2013; Gouras and Ekesten, 2004; Osorio and Vorobyev, 2005; Szél et al., 1992), while co-expression of both opsins (herein either mixed cones or M^+S^+) (Röhlich et al., 1994) broadens the spectral range of individual cones and improves perception under varying conditions of ambient light (Chang et al., 2013).

This unusual opsin expression pattern poses a challenge for color-coding, particularly so for mixed cones. However, it has been discovered that a small population of cones only expresses S-opsin ("true S-cones", or S^+M^-). These true S-cones are thought to be evenly distributed across the retina (Franke et al., 2019; Haverkamp et al., 2005; Szatko et al., 2019; Wang et al., 2011) and to be critical for encoding color, especially in the dorsal retina where they are quasi-evenly distributed in a sea of cones expressing only M-opsin (M^+S^-), a pattern akin to mammalian retinas in general (Haverkamp et al., 2005; Wang et al., 2011). Nonetheless, subsequent physiological studies revealed that color-opponent retinal ganglion cells (RGCs) are more abundant in the dorsal-ventral transition zone (Chang et al., 2013) and the ventral retina (Joesch and Meister, 2016). Recent large scale two-photon imaging results further demonstrated that color opponent cells were mostly located in the ventral retina (Szatko et al., 2019). Intriguingly, a behavior-based mouse study demonstrated that their ability to distinguish color is also restricted to the ventral retina (Denman et al., 2018). These results prompt us to study, at the single-cell level and across the whole retina, the spatial distributions of cone types with different opsin expression configurations and, more importantly, with regard to S-cone bipolar cell connections in order to better understand the anatomical base for the unique color-coding scheme of the mouse retina.

2. RESULTS AND DISCUSSION

2.1. True S-cones are highly concentrated in the ventral retina of pigmented mouse.

2

79   In mouse retina, the gradients of S- and M-opsin expression along the dorsal-ventral axis have
80   been well documented (Figure 1A-B) (Applebury et al., 2000; Calderone and Jacobs, 1995;
81   Chang et al., 2013; Haverkamp et al., 2005; Jelcick et al., 2011; Lyubarsky et al., 1999; Ortín-
82   Martínez et al., 2014; Szél et al., 1992; Wang et al., 2011), but the distribution of individual cone
83   types with different combinations of opsin expression across the whole retina has not been
84   characterized (but see Baden et al., 2013; Eldred et al., 2020, which we discuss below). We
85   developed a highly reliable algorithm to automatically quantify the different opsins (S and M)
86   and cone types (M$^+$S$^-$, true S, and mixed cones, Figure 2, Figure 2- figure supplement 1) based
87   on high-resolution images of entire flat-mount retinas immunolabeled with S- and M-opsin
88   antibodies (Figure 2- figure supplement 1). As demonstrated in examples of opsin labeling from
89   dorsal, medial, and ventral retinal areas of the pigmented mouse (Figure 1B, left), while M
90   opsin-expressing cones (M$^+$: M$^+$S$^+$ + M$^+$S$^-$) were relatively evenly distributed across three regions,
91   S opsin-expressing cones (S$^+$: M$^+$S$^+$ + S$^+$M$^-$) showed considerable anisotropy, with a high density
92   in the ventral retina and a precipitous drop in the dorsal retina, confirming previous
93   observations (Haverkamp et al., 2005; Jelcick et al., 2011; Ortín-Martínez et al., 2014).
94   Surprisingly, instead of finding an even distribution of true S-cones as previously presumed
95   (Baden et al., 2013; Haverkamp et al., 2005; Wang et al., 2011), we found the ventral region
96   had much more numerous true S-cones (~30% of the local cone population; Figure 1C left,
97   Supplementary file 1A) than did the dorsal region (~1%). This result is evident from density
98   maps of cone types from three examples of pigmented mice, showing highly concentrated true
99   S-cones in the ventral retina (Figure 2A, left column, bottom row). In addition, M$^+$S$^-$-cones were
100   concentrated in the dorsal retina, whereas mixed cones dominated the medial and ventral
101   retina (Figure 1C left and Figure 2A, left column, 4th and 5th rows).
102
103   **2.2. Despite the vast difference in S-opsin expression pattern, the distribution of true S-cones**
104   **is strikingly similar between the pigmented and albino mouse.**
105   Such a highly skewed distribution of true S-cones conflicts with the general notion that true S-
106   cones only account for ~5% of cones and are evenly distributed across the mouse retina (Baden
107   et al., 2013; Franke et al., 2019; Haverkamp et al., 2005; Szatko et al., 2019; Wang et al., 2011);
108   however, it is not unprecedented considering the diverse S-cone patterns seen in mammals
109   (Ahnelt et al., 2000; Ahnelt and Kolb, 2000; Calderone et al., 2003; Hendrickson et al., 2000;
110   Hendrickson and Hicks, 2002; Kryger et al., 1998; Müller and Peichl, 1989; Nadal-Nicolás et al.,
111   2018; Ortín-Martínez et al., 2014, 2010; Peichl, 2005; Schiviz et al., 2008; Szél et al., 2000).
112   Therefore, we also examined an albino mouse line to determine whether this observation
113   persists across different mouse strains. Overall, albino retinas had slightly smaller cone
114   populations (Figure 2B, Supplementary file 1B; Ortín-Martínez et al., 2014). Interestingly, while
115   M-opsin expressing cones had similar distributions in both strains, S-opsin expression extended
116   well into the dorsal retina of the albino mouse, exhibiting a greatly reduced gradient of S-opsin
117   expression toward the dorsal retina compared to that seen in pigmented mice (Figure 1B-C,
118   Figure 2A second row; Applebury et al., 2000; Ortín-Martínez et al., 2014). Consequently, most
119   cones in the dorsal retina were mixed cones, and M$^+$S$^-$ cones were very sparse (7%, compared
120   to 97% in pigmented mouse, Figure 1C right, Supplementary file 1A, Figure 2A right). However,
121   despite these differences, the percentage and distribution of true S-cones were remarkably
122   conserved between strains. In both strains, true S-cones were extremely sparse in the dorsal

3

retina (1%) but highly concentrated in the ventral retina (33% vs 29%, Figure 1C and Supplementary file 1A). Notably, the density maps of true S-cones are nearly identical in both strains (Figure 2A, bottom row). Evaluating the distribution of three main cone populations (mixed, M^+S^-, and true S-cone) in four retinal quadrants centered upon the optic nerve head reveals different profiles between pigmented and albino strain for mixed and M^+S^- cones (Figure 2C). For example, in the dorsotemporal (DT) quadrant, we observed an increase of M^+S^- cones from the center to the periphery (green line) in pigmented mice, compared to a majority of mixed cones (gray line) in albino mice. However, true S-cone profiles (magenta lines) were similar between the two strains in all quadrants, except for a slightly increased density along the edge of the ventronasal (VN) quadrant in pigmented mice. A recent study successfully modeled cone opsin expression and type determination according to graded thyroid hormone signaling in a pigmented mouse strain (C57BL/6) (Eldred et al., 2020). It would be interesting to see whether a different pattern of thyroid hormone and/or receptor distribution could recapitulate a similar true S-cone distribution with a very different form of S-opsin expression.

2.3. S-cone bipolar cells exhibit a dorsal-ventral gradient with a higher density in the ventral retina.

One major concern regarding cone classification based on opsin immunolabeling is that some S^+M^- cones may instead be mixed cones with low M-opsin expression (Applebury et al., 2000; Baden et al., 2013; Nikonov et al., 2006; Röhlich et al., 1994). Even though a similar cone-type distributions have been observed in mouse retina, it has been assumed that only a fraction of the S^+M^- cones are 'true' S-cones (Baden et al., 2013; Eldred et al., 2020). Out of caution, S^+M^- cones were only referred to as "anatomical" S-cones due to a lack of confirmation regarding their bipolar connections (Baden et al., 2013). Thus, both true S-cones and S-cone bipolar cells have been generally acknowledged to be evenly distributed across the retina (Haverkamp et al., 2005; Wang et al., 2011; Baden et al., 2013; Szatko et al., 2019; Franke et al., 2019; Eldred et al., 2020). In order to confirm the distribution of true S-cones, it is critical to uncover the distribution and dendritic contacts of S-cone bipolar cells (type 9, or SCBCs). Previously, SCBCs have only been identified among other bipolar, amacrine and ganglion cells in a Thy1-Clomeleon mouse line, rendering the quantification of their distribution across the entire retina impractical (Haverkamp et al., 2005). We generated a Copine9-Venus mouse line, in which SCBCs are specifically marked (Figure 3, Supplementary file 1C), owing to the fact that *Cpne9* is an SCBC-enriched gene (Shekhar et al., 2016). In retinal sections, these Venus$^+$ bipolar cells have axon terminals narrowly ramified in sub-lamina 5 of IPL (Figure 3A), closely resembling type 9 BCs as identified in EM reconstructions (Behrens et al., 2016; Stabio et al., 2018a). In flat-mount view, these bipolar cells are often seen to extend long dendrites to reach true S-cones, bypassing other cone types (Figure 3B-C). The majority of dendritic endings formed enlarged terminals beneath true S-cones pedicles (Figure 3C-c'), but occasional slender "blind" endings were present (arrow in Figure 3C-c"), which have been documented for S-cone bipolar cells in many species (Haverkamp et al., 2005; Herr et al., 2003; Kouyama and Marshak, 1992). Unexpectedly, we found that the distribution of SCBCs was also skewed toward VN retina, albeit with a shallower gradient (Figure 3D-E). To examine the connections between true S-cones and SCBCs, we immunolabeled S- and M-opsins in Copine9-Venus mouse retinas. Because M-opsin antibody signals did not label cone structures other than their outer

167 segments, we first identified true S-cones at the outer segment level and then traced S-opsin
168 labeling to their pedicles in the outer plexiform layer (OPL), where they connect with SCBCs
169 (Figure 3C, for more details see material and methods). Although convergent as well divergent
170 connections were found between true S-cones and SCBCs in both dorsal and ventral retina (see
171 the source data), we noted different connectivity patterns. While in the dorsal retina, a single
172 true S-cone connected to approximately 4 SCBCs (3.8 ± 0.2, see material and methods), in the
173 ventral retina, a single SCBC contacted approximately 5 true S-cones (4.6 ± 0.4; Figure 3C,
174 Supplementary file 2). These results agree well with the true S-cone to SCBC ratios calculated
175 from cell densities in the DT and VN retina. Specifically, in the dorsal retina, the true S-cone to
176 SCBC ratio was approximately 1:3.6, compared to 5.3:1 in the ventral retina (Supplementary file
177 3). Accordingly, both data sets support the presence of a prevalent divergence of true S-cone to
178 SCBC connections in the dorsal retina, in comparison to a prominent convergence of contacts
179 from true S-cones to SCBCs in VN retina. Critically, the specificity of wiring from true S-cones to
180 SCBCs also confirms the identity of true S-cones as revealed by opsin labeling and further
181 supports the finding that true S-cones are highly concentrated in VN mouse retina.
182
183 **2.4. True S-cones in the ventral retina are not evenly distributed but form clusters.**
184 As demonstrated above, in the mouse retina, despite a large population of mixed cones, SCBCs
185 precisely connect with true S-cones, preserving this fundamental mammalian color circuitry
186 motif (Behrens et al., 2016; Breuninger et al., 2011; Haverkamp et al., 2005; Mills et al., 2014).
187 However, the increased density of SCBCs in the ventral retina does not match that of true S-
188 cones (compare Fig 3D and Figure 2a, last row). Thus, individual SCBCs in the ventral retina may
189 be required to develop more dendrites to maximize the number of contacts made with
190 different S-cone terminals (Supplementary file 2, graphs in Figure 3C). Intriguingly, we
191 discovered in both strains that true S-cones in the ventral retina appeared to cluster together
192 rather than forming an even distribution, as revealed by K-nearest neighbor analysis (Figure 4A-
193 B, Supplementary file 2). Ideally, such true S-cone clustering may increase the availability of
194 targets for individual SCBCs in a reduced space.
195
196 To quantify the spatial patterning of true S-cone populations (or their lack thereof), we
197 compared the observed true S-cone distributions within 1-mm diameter VN and DT retinal
198 samples to artificially generated alternative populations (Figure 4C). To this end, we considered
199 two extreme patterning rules: First, one in which the space between true S-cone locations was
200 maximized within the set of actual locations for all cones, creating a relatively uniform (evenly
201 "distributed") mosaic of true S-cones. At the other extreme, cone identities were permuted
202 randomly ("shuffled") among observed cone locations (Figure 4C). Repetition of these
203 algorithms generated distributions of patterning metrics for true S-cones (see below) that
204 remain constrained by the observed cone locations and proportions of cone types for each 1-
205 mm sample.
206
207 To quantitatively compare the patterning of real true S-cone populations to their artificial
208 counterparts, we first computed two measures of regularity for true S-cones: nearest neighbor
209 and Voronoi diagram regularity indices (NNRI and VDRI, respectively; Reese and Keeley, 2015;
210 Figure 4C-D); larger values of these metrics indicate smaller variability in the spacing between

cones and thus more regular patterns. Interestingly, far from being regularly distributed, true S-cone placement was quite irregular and nearly indistinguishable from shuffled populations (including a slight trend toward regularity measures lower than random, which may indicate a tendency toward clustering, Figure 4D; see Reese, 2008). To further probe the possibility of true S-cone clustering, we computed the ratios of true S-cone neighbors for each cone (denoted here as the S-cone neighbor ratio [SCNR]; see Methods for the calculation of the SCNR search radius for each retinal sample). Intriguingly, SCNRs were significantly larger for true S-cones than for other cone types, which were equal to expected ratios due to random chance—especially so in ventral retinas, further indicating a clustering of true S-cones in those areas (Figure 4E). Notably, a more extreme form of clustering of S-cones has been observed in the "wild" mouse (Warwick et al., 2018) and with much lower densities in some felids (Ahnelt et al., 2000). Here, such clustering may reflect the mode of true S-cone development in the ventral retina, for example, by "clonal expansion" to achieve unusually high densities (Bruhn and Cepko, 1996; Reese et al., 1999). It is tempting to speculate that it may also facilitate the wiring of true S-cones with sparsely distributed SCBCs, which were not observed to cluster in the ventral retina (Figure 3E). Indeed, we observed examples of groups of true S-cones forming clusters whose pedicles in the OPL were tightly congregated in a patch and contacted by a nearby SCBC (Figure 4F).

2.5. Enriched true S-cones in the ventral retina may provide an anatomical base for mouse color vision.

Despite being nocturnal and having a rod-dominated retina (Carter-Dawson and LaVail, 1979; Jeon et al., 1998), mice can detect color (Denman et al., 2018; Jacobs et al., 2004). Although it remains uncertain whether the source of long-wavelength sensitive signals for color opponency arises in rods or M-cones (Baden and Osorio, 2019; Ekesten et al., 2000; Ekesten and Gouras, 2005; Joesch and Meister, 2016; Reitner et al., 1991), it is clear that true S-cones provide short-wavelength signals for color discrimination. Given the previously-held notion that true S-cones are evenly distributed across the retina (Baden et al., 2013; Franke et al., 2019; Haverkamp et al., 2005; Szatko et al., 2019; Wang et al., 2011), whereas M^+S^- cones are concentrated in the dorsal retina of pigmented mouse, it is intuitive to speculate that color coding is prevalent in the dorsal retina. However, previous physiological and behavioral studies indicate that, although luminance detection can occur across the mouse retina, color discrimination is restricted to the ventral retina (Breuninger et al., 2011; Denman et al., 2018; Szatko et al., 2019). Thus, our discovery of high enrichment of true S-cones in the ventral retina provides a previously missed anatomical feature for mouse color vision that could help to re-interpret these results. From projections mapping true S-cone densities into visual space (Figure 4-figure supplement 1; Sterratt et al., 2013), it is conceivable that high ventral true S-cone density will provide a much higher sensitivity of short-wavelength signals, thus facilitating color detection for the upper visual field. Although the true S-cone signals carried by SCBCs in the dorsal retina might not be significant for color detection, they could certainly participate in other functions, such as non-image forming vision, that are known to involve short-wavelength signals (Altimus et al., 2008; Doyle et al., 2008; Patterson et al., 2020). Interestingly, the overall true S-cone percentage in the mouse retina remains approximately 10% (Figure 2B), and the average true S-cone to SCBC ratio across the whole retina is about 1.7:1 (Supplementary file 1B-C), similar to

255 what has been reported in other mammals (Ahnelt et al., 2006; Ahnelt and Kolb, 2000; Bumsted
256 et al., 1997; Bumsted and Hendrickson, 1999; Curcio et al., 1991; Hendrickson and Hicks, 2002;
257 Hunt and Peichl, 2014; Kryger et al., 1998; Lukáts et al., 2005; Müller and Peichl, 1989; Ortín-
258 Martínez et al., 2010; Peichl et al., 2000; Schiviz et al., 2008; Shinozaki et al., 2010; Szél et al.,
259 1988).
260
261 Such a spatial rearrangement of true S-cones and SCBCs likely reflects evolutionary adaption to
262 enhance short-wavelength signaling and color coding for the upper visual field as best suited for
263 the habitat and behavior of mice (Baden et al., 2020). For example, it may facilitate aerial
264 predator detection during daytime (Yilmaz and Meister, 2013). Similarly, skewed S-cone
265 arrangement has been reported for other terrestrial prey mammals (Famiglietti and Sharpe,
266 1995; Juliusson et al., 1994; Röhlich et al., 1994), while zebrafish possess a UV-enriched ventral
267 retina that enhances their predation (Zimmermann et al., 2018). In addition, we observed that
268 the clustering of true S-cones in the ventral retina may allow several neighboring cones of the
269 same type to converge onto the same SCBC (Figure 4F), which could potentially enhance signal-
270 to-noise ratios for more accurate detection, as described recently in human fovea (Schmidt et
271 al., 2019). It is also remarkable that despite the very different S-opsin expression patterns in
272 both mouse strains, the true S-cone population and distribution are strikingly similar between
273 pigmented and albino mice, suggesting a common functional significance.
274
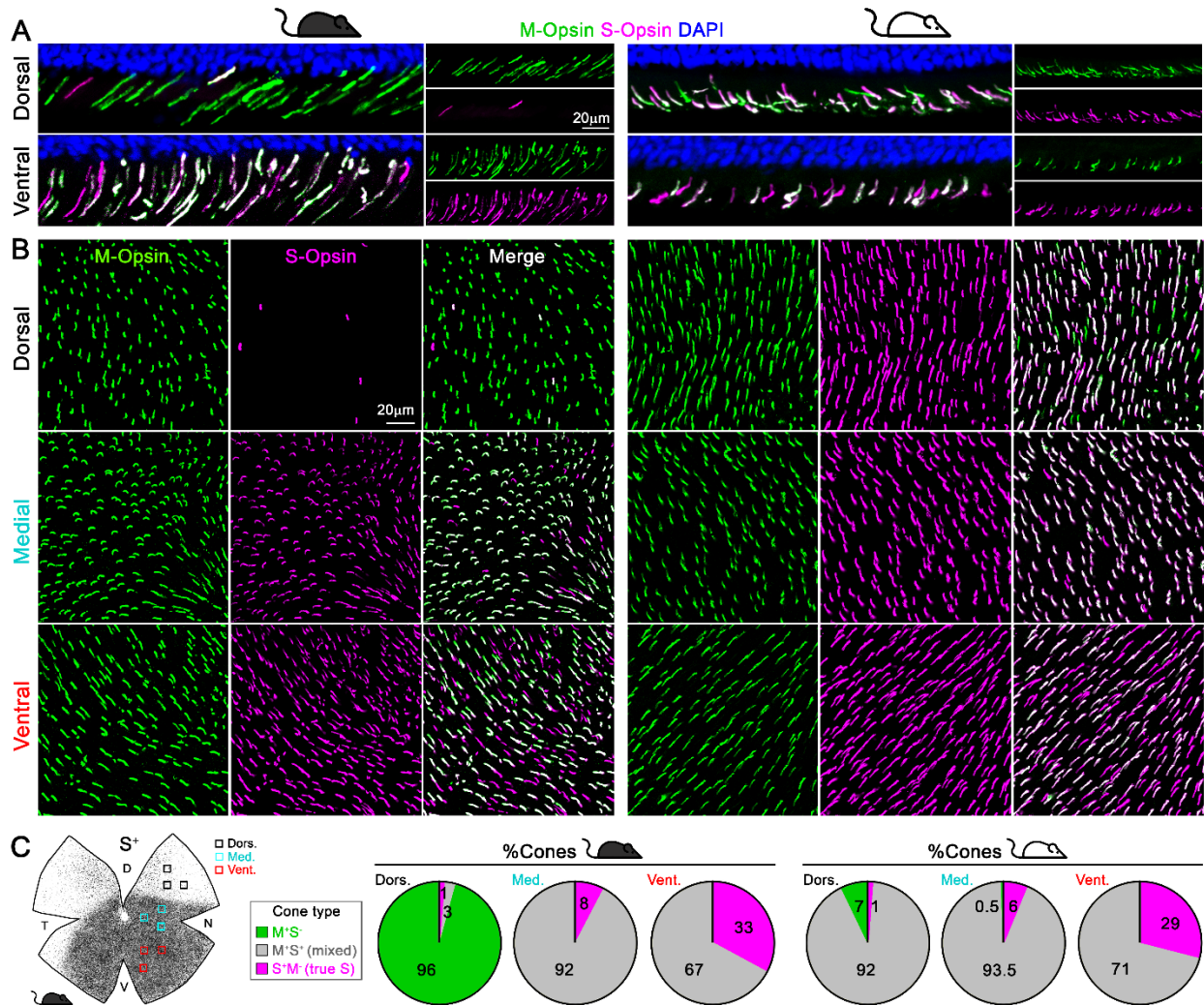
6. FIGURES

Figure 1. Cone outer segments across retinal areas. Immunodetection of M and S wavelength-sensitive opsins in retinal sections (A) and flat-mount retinas (B) in two mouse strains (pigmented and albino mice, left and right columns respectively). (C) Retinal scheme of S-opsin expression used for image sampling to quantify and classify cones in three different retinal regions. Pie graphs showing the percentage of cones manually classified as M^+S^- (green), S^+M^- (true S, magenta) and M^+S^+ (mixed, gray) based on the opsin expression in different retinal areas from four retinas per strain. Black mouse: pigmented mouse strain (C57BL6), white mouse: albino mouse strain (CD1).
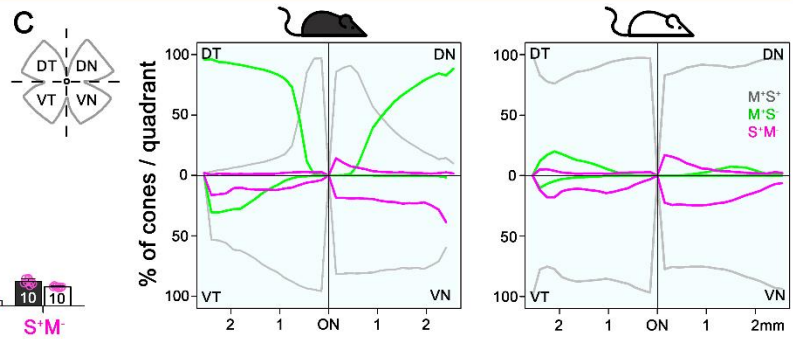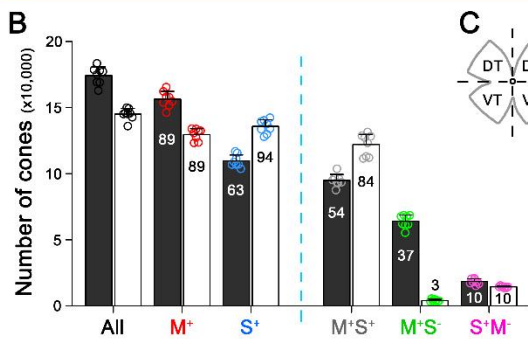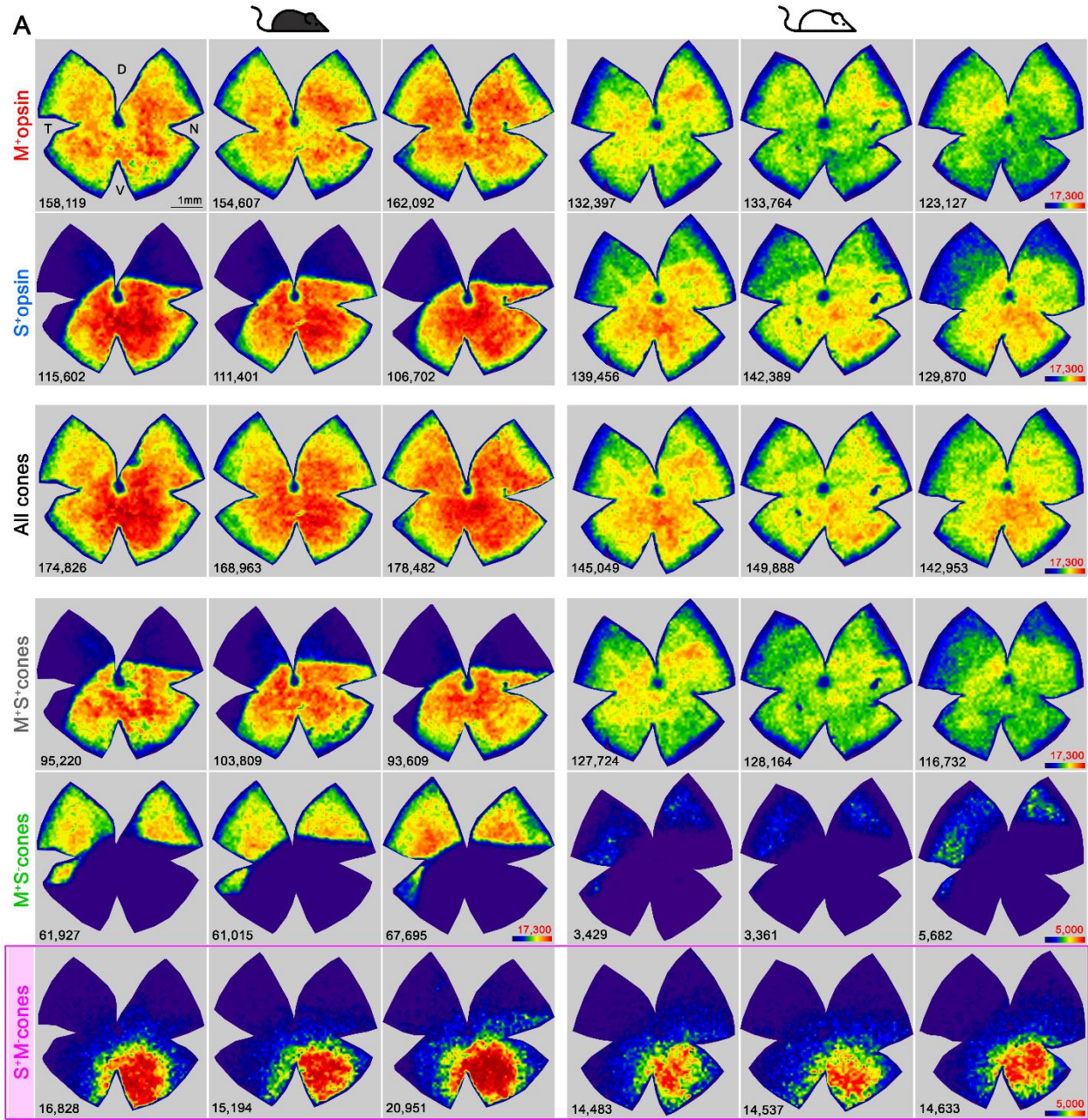
Figure 2. Topography and total number of different opsins (M⁺, S⁺) and cone-type populations in the whole mouse retina. (A) Density maps depicting the distributions of different opsins

299   expressing cones (M^+ and S^+) and different cone populations classified anatomically as: All, M^+S^+
300   (mixed), M^+S^-, S^+M^- (true S) cones in pigmented and albino mice (left and right side respectively).
301   Each column shows different cone populations from the same retina and, at the bottom of each
302   map is shown the number of quantified cones. Color scales are shown in the right panel of each
303   row (from 0 [purple] to 17,300 [dark red] for all cone types except to 5,000 cones/mm^2 [dark
304   red] for the true S-cones and M^+S^--cone in the albino strain). Retinal orientation depicted by D:
305   dorsal, N: nasal, T: temporal, V: ventral. (B) Histogram showing the mean ± standard deviation
306   of different cone subtypes for eight retinas per strain (Supplementary file 1B). The percentages
307   of each cone subtype are indicated inside of each bar, where 100% indicates the total of the 'all
308   cones' group. (C) Opsin expression profile across the different retinal quadrants (retinal scheme,
309   DT: dorsotemporal, DN: dorsonasal, VT: ventrotemporal, VN: ventronasal). Line graphs show
310   the spatial profile of relative opsins expression (mixed [gray], M^+S^- [green], true S-cones
311   [magenta]), where the sum of these three cone populations at a given distance from the optic
312   nerve (ON) head equals 100%. Black mouse: pigmented mouse strain, white mouse: albino
313   mouse strain.
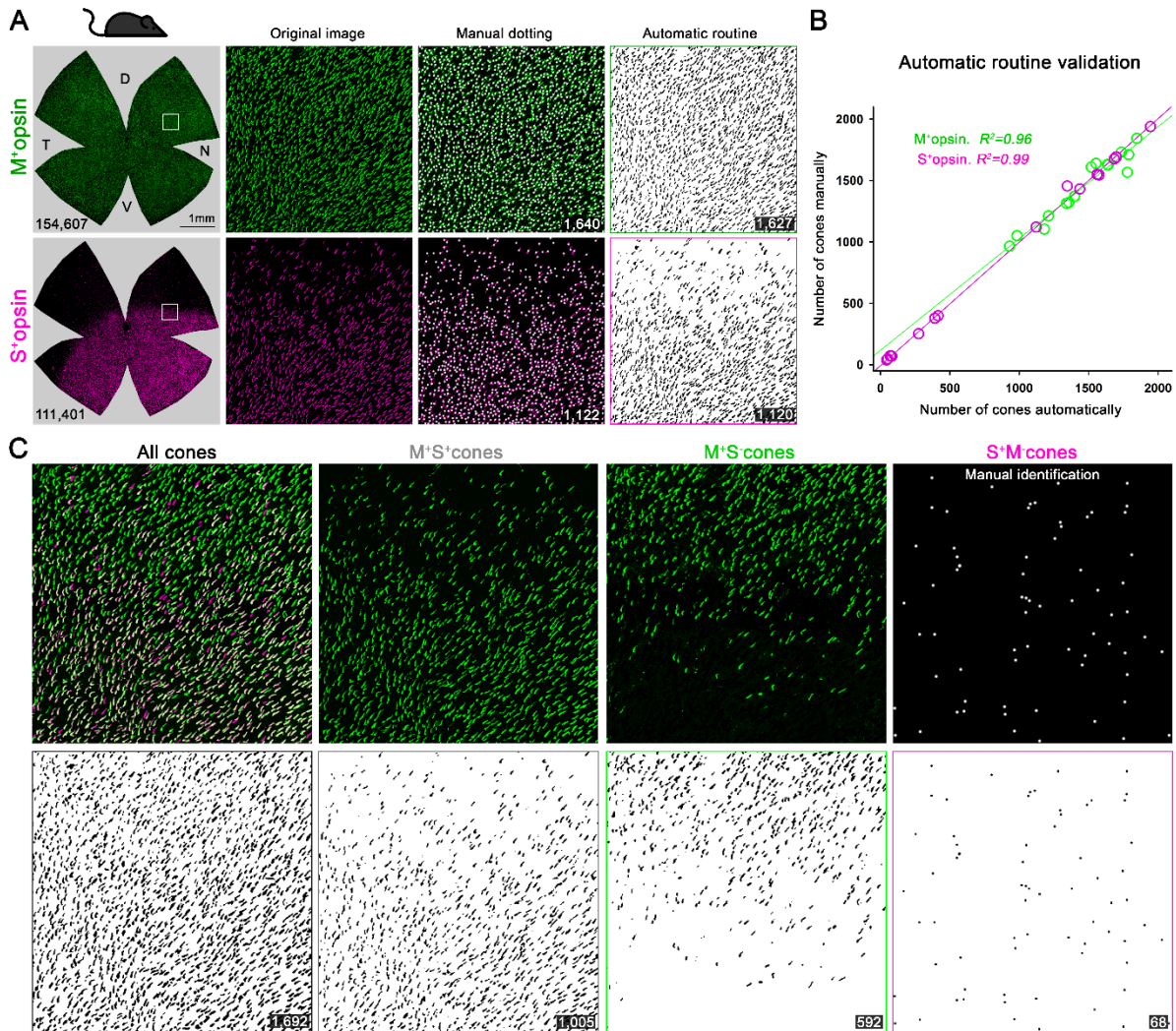
314
315 Figure 2-figure supplement 1. Validation of automatic routine for cone outer segment
316 quantification. (A) Retinal photomontages for M- and S-opsin signal in the same pigmented
317 retina (correspond to second column in Figure 2A). The square depicts an area of interest
318 selected (transition zone of S-opsin expression) to perform the automatic routine validation by
319 comparing manual and automatic quantifications. The images processed by the automatic
320 routine using ImageJ show the selection of positive objects from the corresponding original
321 image. (B) X, Y graph showing the linear correlation (Pearson coefficient, R^2) between manual
322 and automatic quantifications. 21,898 M^+ and 13,705 S^+cones were manually annotated while
323 21,689 M^+ and 13,661 S^+cones were automatically identified in 3 random images obtained from
324 5 retinal photomontages. (C) All, mixed, M^+S^-- and true S-cone populations are extracted from
325 the original M- and S-cone images. All-cones were quantified after overlapping M- and S-signals.
326 mixed (M^+S^+) cones were obtained by subtracting the background of the S-opsin image in the
327 M-opsin one. M^+S^- cones for pigmented mice are obtained after subtracting the S-opsin signal
328 to the M-opsin photomontage. Finally, M^+S^- cones for albino and true S-cones (S^+M^-), in both
329 strains, are manually marked on the retinal photomontage (Adobe Photoshop CC). The B&W
330 images shown the processed image after quantifying automatically. At the bottom of each
331 image is shown the number of quantified cones. Black mouse: pigmented mouse strain.

332
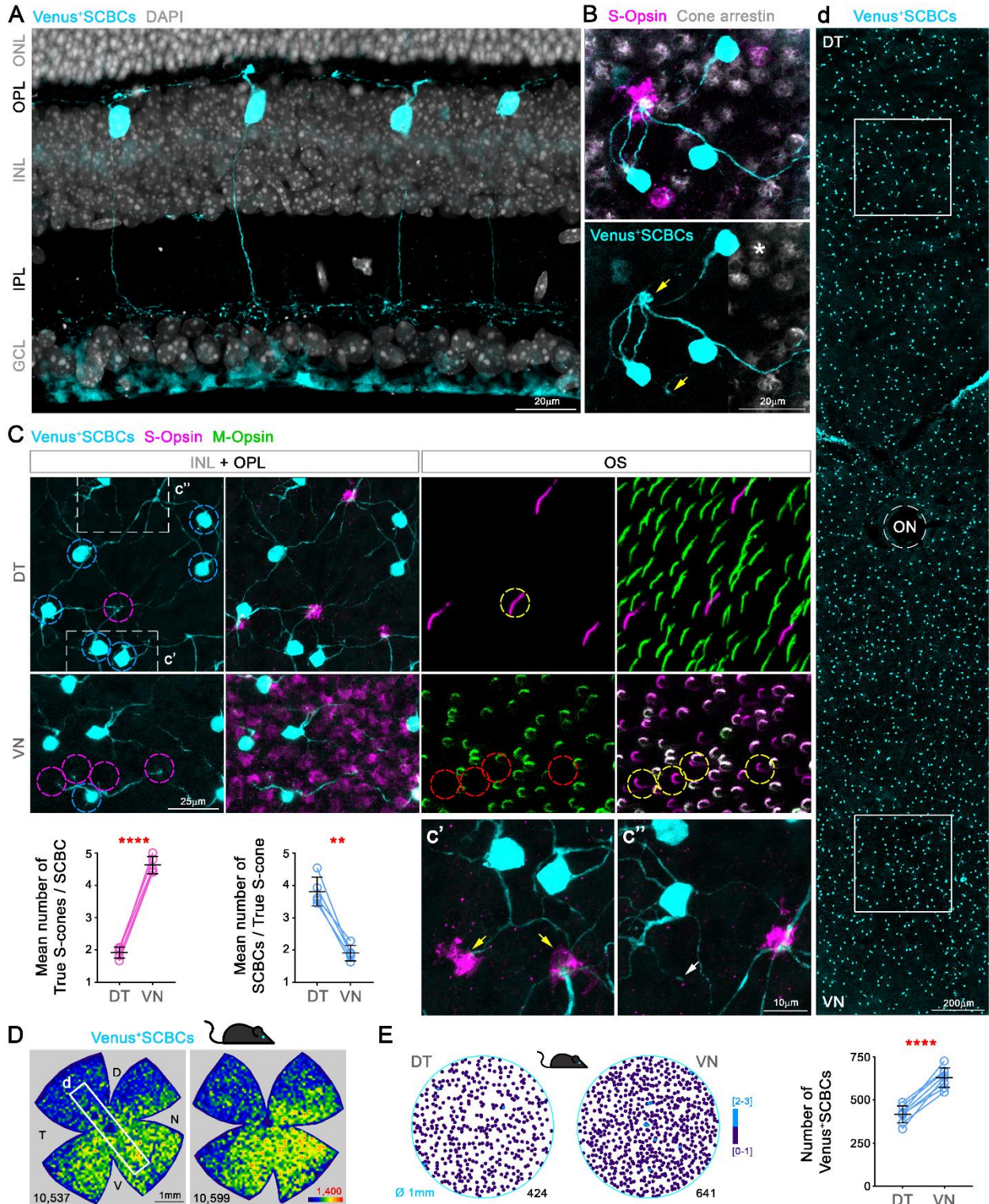
Figure 3. S-cone Bipolar cells (SCBCs) in Cpne9-Venus mouse retina. (A) Retinal cross section showing the characteristic morphology of SCBCs (Behrens et al., 2016; Breuninger et al., 2011). (B) Detailed view of the selective connectivity between Venus[+]SCBCs and true S-cone terminals (yellow arrows). Note that SCBCs avoid contacts with cone terminals lacking S-opsin expression

337   (M^+S^--cone pedicles, identified using cone arrestin), as well as a mixed cone pedicle, marked
338   with an asterisk. In fact, on the contrary, the SCBCs prefer to develop multiple contacts to the
339   same true S-cone pedicle. (C) Images from flat-mount retinas focused on the inner nuclear and
340   outer plexiform layers (INL+OPL) or in the photoreceptor outer segment (OS) layer of the
341   corresponding area. Magnifications showing divergent and convergent connectivity patterns
342   from true S-cone pedicles in dorsal and ventral retinal domains, respectively. In the DT retina,
343   six Venus$^+$ SCBCs (cyan circles) contact a single true S-cone pedicle (magenta circle in DT); while
344   one Venus$^+$ SCBC contacts at least four true S-cone pedicles in the VN retina (magenta circles in
345   VN), which belong to cones possessing S^+M^-OSs (yellow circles). Connectivity between true S-
346   cones and SCBCs in DT and VN retina was assessed as the average number of true S-cone
347   pedicles contacting a single SCBC per retina (magenta plot) or the average number of SCBCs
348   contacting a single true S-cone pedicle per retina (cyan plot) ($p<0.0001$, $p<0.01$, respectively;
349   n=5). (c') Detailed view of a secondary SCBC bifurcation contacting independently two true S-
350   cone pedicles. (c") Detailed view of a "blind" SCBC process. (D) Density maps depicting the
351   distributions of SCBCs in Cpne9-Venus mice. (d) Venus$^+$ SCBCs along the DT-VN axis from a flat-
352   mount retina (corresponding to the white frame in D) showing the gradual increase of SCBCs
353   towards the VN retina where true S-cone density peaks (last row in Figure 2A). (E)
354   Demonstration of Venus$^+$ SCBC densities color-coded by the k-nearest neighbor algorithm
355   according to the number of other Venus$^+$ SCBCs found within an 18 μm radius in two circular
356   areas of interest (DT and VN). Although, Venus$^+$ SCBCs exhibit a sparse density without forming
357   clusters (circular maps), they were significantly denser in VN retina ($p<0.0001$; n=8).
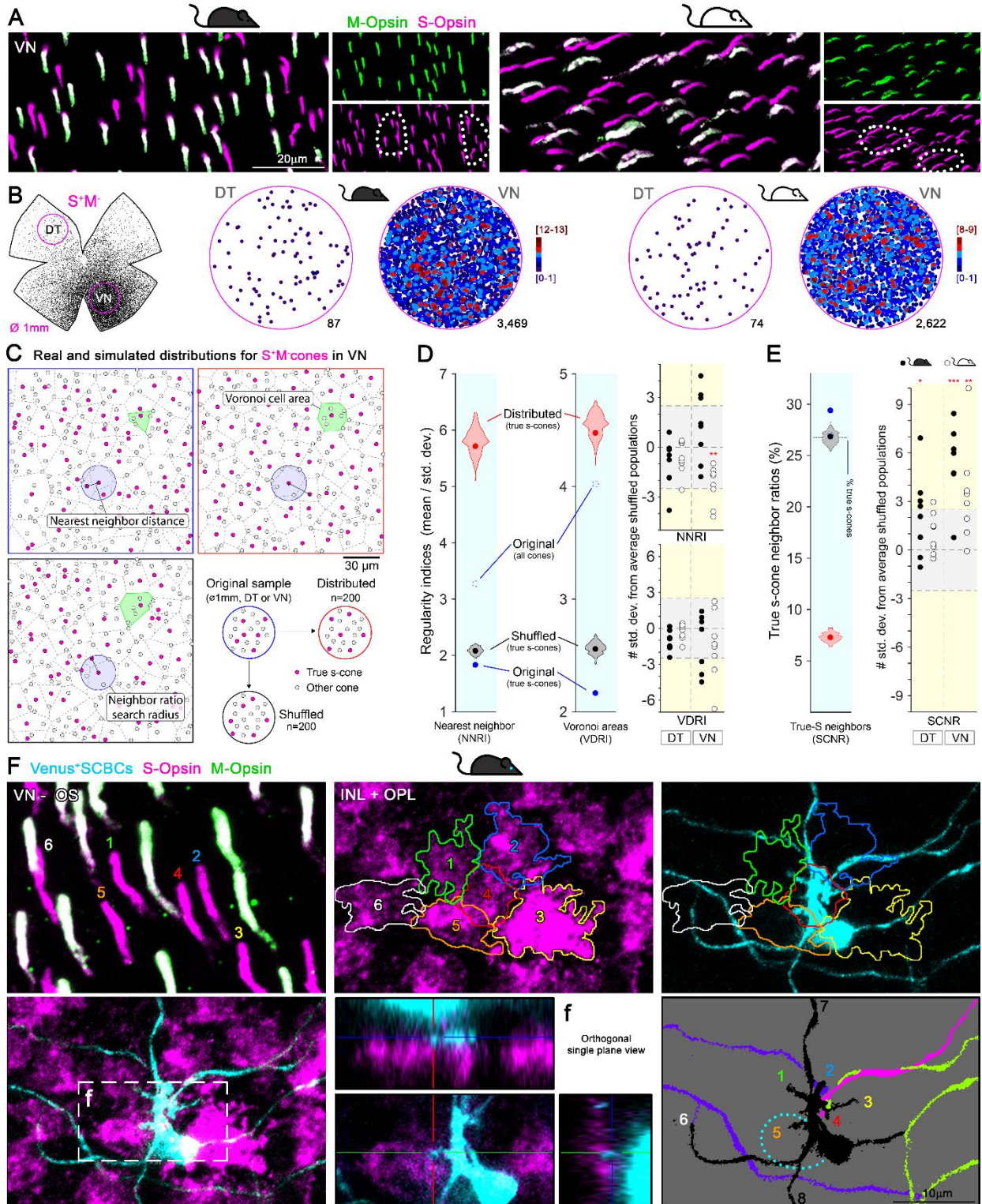
Figure 4. Clustering of true S-cones in the ventronasal (VN) retina. (A) Retinal magnifications from flat-mount retinas demonstrating grouping of true S-cones in the VN area, where true S-cone density peaks. White dashed lines depict independent groups of true S-cones that are not commingled with mixed cones (M^+S^+, white outer segments in the merged image). (B) Retinal

14

scheme of true S-cones used for selecting two circular areas of interest along the dorsotemporal-ventronasal (DT-VN) axis. Circular maps demonstrate true S-cone clustering in these regions. True S-cone locations are color-coded by the k-nearest neighbor algorithm according to the number of other true S-cones found within an 18 μm radius. (C-E) Analytical comparisons of DT and VN populations of true S-cones to their simulated alternatives. C) Example real and simulated true S-cone populations and their quantification. Images depict true S-cone locations (magenta dots) and boundaries of their Voronoi cells (dashed lines) from original and example simulated ("distributed", "shuffled") cone populations. Gray dots indicate the locations of other cone types. Observed cone locations were used for all simulated populations; only their cone identities were changed. The annotated features are examples of those measurements used in the calculations presented in D-E. (D) Comparison of sample regularity indices for one albino VN retinal sample to violin plots of those values observed for n=200 simulated cone populations. Note that average regularity indices for true S-cones were lower than that of shuffled populations, whereas those values lay between shuffled and distributed populations when all cones were considered. Plots on the right show values for all actual retinal samples normalized using the mean and standard deviations of their simulated "shuffled" counterparts. The y-axis range corresponding to ± 2.5 standard deviations from the mean (i.e., that containing ~99% of shuffled samples) is highlighted in gray. (E) Comparison of the real average SCNR for the example in C-D to those values for its simulated counterparts. Note that the average SCNR for all cones in this sample was equal to that predicted by random chance (i.e., the ratio of true S-cones to all cones), which in turn was equal to the average for true S-cones for shuffled samples. In contrast, the real true S-cone SCNR was higher. Plot on the right shows true S-cone SCNR values for all samples, normalized as described for D. (F) Convergent connectivity from a true S-cone cluster to a single SCBC in the VN retina. Images of a true S-cone cluster, in a flat-mount retina, focused on the photoreceptor outer segment layer and the inner nuclear-outer plexiform layers (INL+OPL). The upper left panel show the numerical and colored identification of each true S-outer segment in the cluster (note that the number positions indicate the locations where outer segments contact the photoreceptor inner segment). Each true S-cone pedicle belonging to this cluster is outlined and color coded (middle upper panel) and are overlaid upon the SCBC dendritic profile (right upper panel). To identify synaptic contacts between the SCBC and the cone pedicles (maximum intensity projection - excluding the SCBC soma- shown in lower left panel), we acquired orthogonal single plane views zooming into putative dendritic tips. An example for the contact with cone #5 is shown in lower middle panel, corresponding to the box area in lower left panel (f). The lower right panel shows dendritic endings of this SBCB (black) contacting the marked cones (#1-6). It also contacts two additional cones outside of the field of view (#7,8). Dashed line depicts the soma of the SCBC. Dendrites from other SCBCs are color coded for differentiation.

400
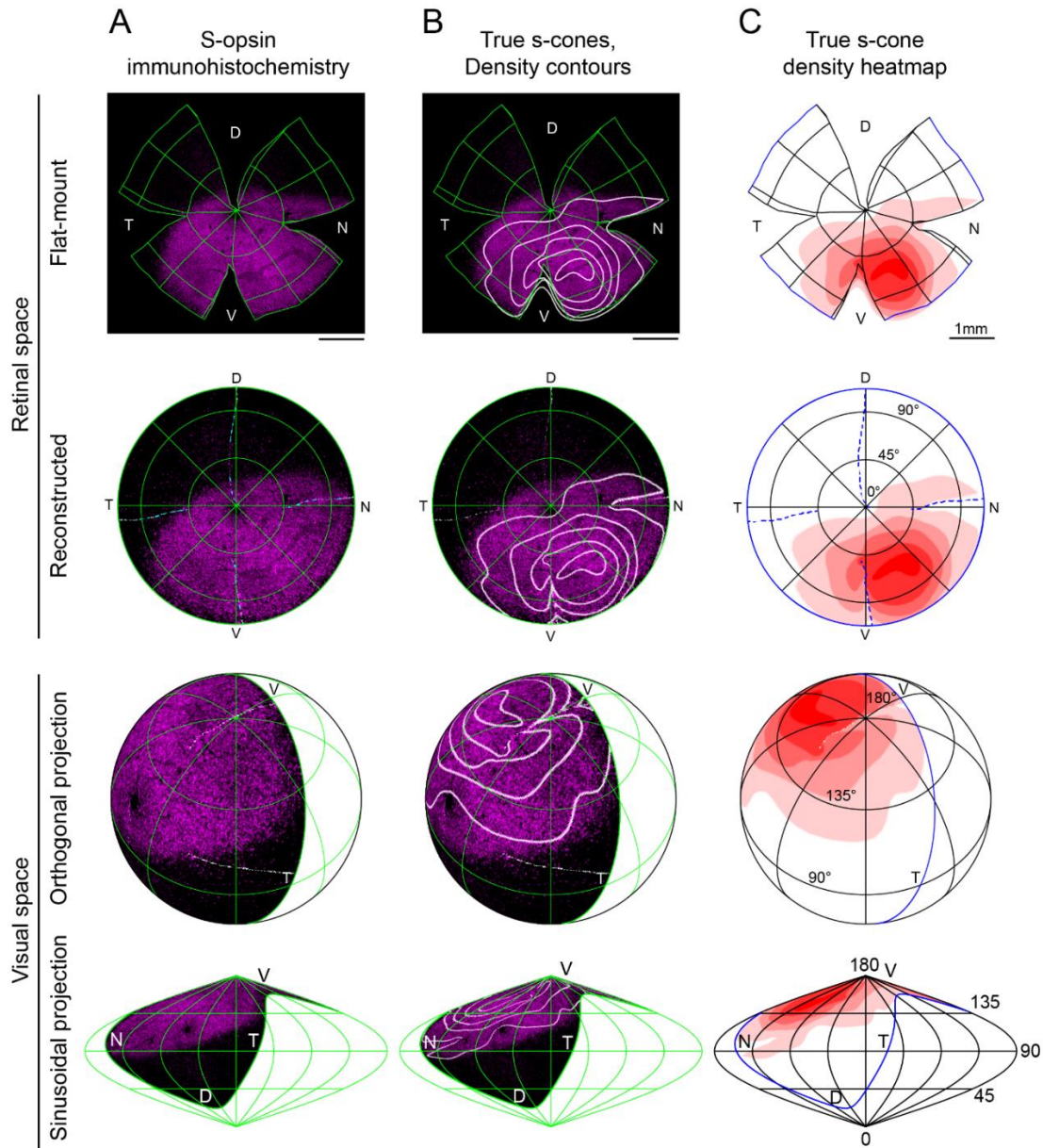
Figure 4-figure supplement 1. Reconstruction and mapping of true S-cone densities into visual space. Representative left eye from a 3-month-old pigmented mouse (C57). (A) S-opsin antibody labeling; (B) true s-cone density contour lines separated by quintiles overlaid onto s-opsin labeling; (C) quintile heatmap contours of true s-cone density. The top two rows demonstrate the flat-mount retina with marks for edges and relaxing cuts, followed by its reconstruction into uncut retinal space with lines of latitude and longitude that have been projected onto the flat-mount. The bottom two rows show the reconstructed retina inverted into visual space using orthogonal and sinusoidal projections. For these views, eye orientation angles for elevation and azimuth of 22° and 64°, respectively, have been used as in (Sterratt et al., 2013). For orthogonal projections, the globe has been rotated forward by 50° to emphasize the relationship of true S-cone densities to the upper pole of the visual field. S-opsin labeling is restricted to the upper visual field, but true S-cones are concentrated toward its lateral edges.

16

7. REFERENCES

Ahnelt PK, Fernández E, Martinez O, Bolea JA, Kübber-Heiss A. 2000. Irregular S-cone mosaics in felid retinas. Spatial interaction with axonless horizontal cells, revealed by cross correlation. *J Opt Soc Am A Opt Image Sci Vis* **17**:580–588. doi:10.1364/josaa.17.000580

Ahnelt PK, Kolb H. 2000. The mammalian photoreceptor mosaic-adaptive design. *Prog Retin Eye Res* **19**:711–777. doi:10.1016/s1350-9462(00)00012-4

Ahnelt PK, Schubert C, Kübber-Heiss A, Schiviz A, Anger E. 2006. Independent variation of retinal S and M cone photoreceptor topographies: A survey of four families of mammals. *Vis Neurosci* **23**:429–435. doi:10.1017/S095252380623342X

Altimus CM, Güler AD, Villa KL, McNeill DS, Legates TA, Hattar S. 2008. Rods-cones and melanopsin detect light and dark to modulate sleep independent of image formation. *Proc Natl Acad Sci USA* **105**:19998–20003. doi:10.1073/pnas.0808312105

Applebury ML, Antoch MP, Baxter LC, Chun LL, Falk JD, Farhangfar F, Kage K, Krzystolik MG, Lyass LA, Robbins JT. 2000. The murine cone photoreceptor: a single cone type expresses both S and M opsins with retinal spatial patterning. *Neuron* **27**:513–523. doi:10.1016/s0896-6273(00)00062-3

Baden T, Euler T, Berens P. 2020. Understanding the retinal basis of vision across species. *Nat Rev Neurosci* **21**:5–20. doi:10.1038/s41583-019-0242-1

Baden T, Osorio D. 2019. The Retinal Basis of Vertebrate Color Vision. *Annu Rev Vis Sci* **5**:177–200. doi:10.1146/annurev-vision-091718-014926

Baden T, Schubert T, Chang L, Wei T, Zaichuk M, Wissinger B, Euler T. 2013. A tale of two retinal domains: near-optimal sampling of achromatic contrasts in natural scenes through asymmetric photoreceptor distribution. *Neuron* **80**:1206–1217. doi:10.1016/j.neuron.2013.09.030

Behrens C, Schubert T, Haverkamp S, Euler T, Berens P. 2016. Connectivity map of bipolar cells and photoreceptors in the mouse retina. *Elife* **5**. doi:10.7554/eLife.20041

Breuninger T, Puller C, Haverkamp S, Euler T. 2011. Chromatic bipolar cell pathways in the mouse retina. *J Neurosci* **31**:6504–6517. doi:10.1523/JNEUROSCI.0616-11.2011

Bruhn SL, Cepko CL. 1996. Development of the pattern of photoreceptors in the chick retina. *J Neurosci* **16**:1430–1439.

Bumsted K, Hendrickson A. 1999. Distribution and development of short-wavelength cones differ between Macaca monkey and human fovea. *J Comp Neurol* **403**:502–516.

Bumsted K, Jasoni C, Szél A, Hendrickson A. 1997. Spatial and temporal expression of cone opsins during monkey retinal development. *J Comp Neurol* **378**:117–134.

Calderone JB, Jacobs GH. 1995. Regional variations in the relative sensitivity to UV light in the mouse retina. *Vis Neurosci* **12**:463–468. doi:10.1017/s0952523800008361

Calderone JB, Reese BE, Jacobs GH. 2003. Topography of photoreceptors and retinal ganglion cells in the spotted hyena (Crocuta crocuta). *Brain Behav Evol* **62**:182–192. doi:10.1159/000073270

Carter-Dawson LD, LaVail MM. 1979. Rods and cones in the mouse retina. I. Structural analysis using light and electron microscopy. *J Comp Neurol* **188**:245–262. doi:10.1002/cne.901880204

456 Chang L, Breuninger T, Euler T. 2013. Chromatic coding from cone-type unselective circuits in
457   the mouse retina. *Neuron* **77**:559–571. doi:10.1016/j.neuron.2012.12.012
458 Curcio CA, Allen KA, Sloan KR, Lerea CL, Hurley JB, Klock IB, Milam AH. 1991. Distribution and
459   morphology of human cone photoreceptors stained with anti-blue opsin. *J Comp Neurol*
460   **312**:610–624. doi:10.1002/cne.903120411
461 Denman DJ, Luviano JA, Ollerenshaw DR, Cross S, Williams D, Buice MA, Olsen SR, Reid RC. 2018.
462   Mouse color and wavelength-specific luminance contrast sensitivity are non-uniform
463   across visual space. *Elife* **7**. doi:10.7554/eLife.31209
464 Dominy NJ, Lucas PW. 2001. Ecological importance of trichromatic vision to primates. *Nature*
465   **410**:363–366. doi:10.1038/35066567
466 Doyle SE, Yoshikawa T, Hillson H, Menaker M. 2008. Retinal pathways influence temporal niche.
467   *Proc Natl Acad Sci USA* **105**:13133–13138. doi:10.1073/pnas.0801728105
468 Ekesten B, Gouras P. 2005. Cone and rod inputs to murine retinal ganglion cells: evidence of
469   cone   opsin   specific   channels.   *Vis   Neurosci*   **22**:893–903.
470   doi:10.1017/S0952523805226172
471 Ekesten B, Gouras P, Yamamoto S. 2000. Cone inputs to murine retinal ganglion cells. *Vision Res*
472   **40**:2573–2577. doi:10.1016/s0042-6989(00)00122-x
473 Eldred KC, Avelis C, Jr RJJ, Roberts E. 2020. Modeling binary and graded cone cell fate
474   patterning   in   the   mouse   retina.   *PLOS   Computational   Biology*   **16**:e1007691.
475   doi:10.1371/journal.pcbi.1007691
476 Famiglietti EV, Sharpe SJ. 1995. Regional topography of rod and immunocytochemically
477   characterized "blue" and "green" cone photoreceptors in rabbit retina. *Vis Neurosci*
478   **12**:1151–1175. doi:10.1017/s0952523800006799
479 Franke K, Maia Chagas A, Zhao Z, Zimmermann MJ, Bartel P, Qiu Y, Szatko KP, Baden T, Euler T.
480   2019. An arbitrary-spectrum spatial visual stimulator for vision research. *Elife* **8**.
481   doi:10.7554/eLife.48779
482 Gerl EJ, Morris MR. 2008. The Causes and Consequences of Color Vision. *Evo Edu Outreach*
483   **1**:476–486. doi:10.1007/s12052-008-0088-x
484 Gouras P, Ekesten B. 2004. Why do mice have ultra-violet vision? *Exp Eye Res* **79**:887–892.
485   doi:10.1016/j.exer.2004.06.031
486 Haverkamp S, Wässle H, Duebel J, Kuner T, Augustine GJ, Feng G, Euler T. 2005. The primordial,
487   blue-cone   color   system   of   the   mouse   retina.   *J   Neurosci*   **25**:5438–5445.
488   doi:10.1523/JNEUROSCI.1117-05.2005
489 Hendrickson A, Djajadi HR, Nakamura L, Possin DE, Sajuthi D. 2000. Nocturnal tarsier retina has
490   both short and long/medium-wavelength cones in an unusual topography. *J Comp
491   Neurol* **424**:718–730. doi:10.1002/1096-9861(20000904)424:4<718::aid-cne12>3.0.co;2-
492   z
493 Hendrickson A, Hicks D. 2002. Distribution and density of medium- and short-wavelength
494   selective   cones   in   the   domestic   pig   retina.   *Exp   Eye   Res*   **74**:435–444.
495   doi:10.1006/exer.2002.1181
496 Herr S, Klug K, Sterling P, Schein S. 2003. Inner S-cone bipolar cells provide all of the central
497   elements   for   S   cones   in   macaque   retina.   *J   Comp   Neurol*   **457**:185–201.
498   doi:10.1002/cne.10553

499   Hunt DM, Peichl L. 2014. S cones: Evolution, retinal distribution, development, and spectral
500   sensitivity. *Vis Neurosci* **31**:115–138. doi:10.1017/S0952523813000242
501   Jacobs GH. 1993. The distribution and nature of colour vision among the mammals. *Biol Rev*
502   *Camb Philos Soc* **68**:413–471. doi:10.1111/j.1469-185x.1993.tb00738.x
503   Jacobs GH, Neitz J, Deegan JF. 1991. Retinal receptors in rodents maximally sensitive to
504   ultraviolet light. *Nature* **353**:655–656. doi:10.1038/353655a0
505   Jacobs GH, Neitz M, Deegan JF, Neitz J. 1996. Trichromatic colour vision in New World monkeys.
506   *Nature* **382**:156–158. doi:10.1038/382156a0
507   Jacobs GH, Williams GA, Fenwick JA. 2004. Influence of cone pigment coexpression on spectral
508   sensitivity and color vision in the mouse. *Vision Res* **44**:1615–1622.
509   doi:10.1016/j.visres.2004.01.016
510   Jelcick AS, Yuan Y, Leehy BD, Cox LC, Silveira AC, Qiu F, Schenk S, Sachs AJ, Morrison MA,
511   Nystuen AM, DeAngelis MM, Haider NB. 2011. Genetic variations strongly influence
512   phenotypic outcome in the mouse retina. *PLoS ONE* **6**:e21858.
513   doi:10.1371/journal.pone.0021858
514   Jeon CJ, Strettoi E, Masland RH. 1998. The major cell populations of the mouse retina. *J*
515   *Neurosci* **18**:8936–8946.
516   Joesch M, Meister M. 2016. A neuronal circuit for colour vision based on rod-cone opponency.
517   *Nature* **532**:236–239. doi:10.1038/nature17158
518   Juliusson B, Bergström A, Röhlich P, Ehinger B, van Veen T, Szél A. 1994. Complementary cone
519   fields of the rabbit retina. *Invest Ophthalmol Vis Sci* **35**:811–818.
520   Kouyama N, Marshak DW. 1992. Bipolar cells specific for blue cones in the macaque retina. *J*
521   *Neurosci* **12**:1233–1252.
522   Kryger Z, Galli-Resta L, Jacobs GH, Reese BE. 1998. The topography of rod and cone
523   photoreceptors in the retina of the ground squirrel. *Vis Neurosci* **15**:685–691.
524   doi:10.1017/s0952523898154081
525   Lukáts A, Szabó A, Röhlich P, Vígh B, Szél A. 2005. Photopigment coexpression in mammals:
526   comparative and developmental aspects. *Histol Histopathol* **20**:551–574.
527   doi:10.14670/HH-20.551
528   Lyubarsky AL, Falsini B, Pennesi ME, Valentini P, Pugh EN. 1999. UV- and midwave-sensitive
529   cone-driven retinal responses of the mouse: a possible phenotype for coexpression of
530   cone photopigments. *J Neurosci* **19**:442–455.
531   Marshak DW, Mills SL. 2014. Short-wavelength cone-opponent retinal ganglion cells in
532   mammals. *Vis Neurosci* **31**:165–175. doi:10.1017/S095252381300031X
533   Mills SL, Tian L-M, Hoshi H, Whitaker CM, Massey SC. 2014. Three distinct blue-green color
534   pathways in a mammalian retina. *J Neurosci* **34**:1760–1768.
535   doi:10.1523/JNEUROSCI.3901-13.2014
536   Müller B, Peichl L. 1989. Topography of cones and rods in the tree shrew retina. *J Comp Neurol*
537   **282**:581–594. doi:10.1002/cne.902820409
538   Nadal-Nicolás FM, Salinas-Navarro M, Jiménez-López M, Sobrado-Calvo P, Villegas-Pérez MP,
539   Vidal-Sanz M, Agudo-Barriuso M. 2014. Displaced retinal ganglion cells in albino and
540   pigmented rats. *Front Neuroanat* **8**:99. doi:10.3389/fnana.2014.00099
541   Nadal-Nicolás FM, Vidal-Sanz M, Agudo-Barriuso M. 2018. The aging rat retina: from function to
542   anatomy. *Neurobiol Aging* **61**:146–168. doi:10.1016/j.neurobiolaging.2017.09.021

543 Nathans J, Thomas D, Hogness DS. 1986. Molecular genetics of human color vision: the genes
544   encoding blue, green, and red pigments. *Science* **232**:193–202.
545   doi:10.1126/science.2937147

546 Ng L, Hurley JB, Dierks B, Srinivas M, Saltó C, Vennström B, Reh TA, Forrest D. 2001. A thyroid
547   hormone receptor that is required for the development of green cone photoreceptors.
548   *Nat Genet* **27**:94–98. doi:10.1038/83829

549 Nikonov SS, Kholodenko R, Lem J, Pugh EN. 2006. Physiological features of the S- and M-cone
550   photoreceptors of wild-type mice from single-cell recordings. *J Gen Physiol* **127**:359–374.
551   doi:10.1085/jgp.200609490

552 Ortín-Martínez A, Jiménez-López M, Nadal-Nicolás FM, Salinas-Navarro M, Alarcón-Martínez L,
553   Sauvé Y, Villegas-Pérez MP, Vidal-Sanz M, Agudo-Barriuso M. 2010. Automated
554   quantification and topographical distribution of the whole population of S- and L-cones
555   in adult albino and pigmented rats. *Invest Ophthalmol Vis Sci* **51**:3171–3183.
556   doi:10.1167/iovs.09-4861

557 Ortín-Martínez A, Nadal-Nicolás FM, Jiménez-López M, Alburquerque-Béjar JJ, Nieto-López L,
558   García-Ayuso D, Villegas-Pérez MP, Vidal-Sanz M, Agudo-Barriuso M. 2014. Number and
559   distribution of mouse retinal cone photoreceptors: differences between an albino (Swiss)
560   and a pigmented (C57/BL6) strain. *PLoS ONE* **9**:e102392.
561   doi:10.1371/journal.pone.0102392

562 Osorio D, Vorobyev M. 2005. Photoreceptor spectral sensitivities in terrestrial animals:
563   adaptations for luminance and colour vision. *Proc Biol Sci* **272**:1745–1752.
564   doi:10.1098/rspb.2005.3156

565 Patterson SS, Kuchenbecker JA, Anderson JR, Neitz M, Neitz J. 2020. A Color Vision Circuit for
566   Non-Image-Forming Vision in the Primate Retina. *Curr Biol*.
567   doi:10.1016/j.cub.2020.01.040

568 Peichl L. 2005. Diversity of mammalian photoreceptor properties: adaptations to habitat and
569   lifestyle? *Anat Rec A Discov Mol Cell Evol Biol* **287**:1001–1012. doi:10.1002/ar.a.20262

570 Peichl L, Künzle H, Vogel P. 2000. Photoreceptor types and distributions in the retinae of
571   insectivores. *Vis Neurosci* **17**:937–948. doi:10.1017/s0952523800176138

572 Puller C, Haverkamp S. 2011. Bipolar cell pathways for color vision in non-primate dichromats.
573   *Vis Neurosci* **28**:51–60. doi:10.1017/S0952523810000271

574 Reese BE. 2008. 1.22 - Mosaics, Tiling, and Coverage by Retinal Neurons In: Masland RH,
575   Albright TD, Albright TD, Masland RH, Dallos P, Oertel D, Firestein S, Beauchamp GK,
576   Catherine Bushnell M, Basbaum AI, Kaas JH, Gardner EP, editors. The Senses: A
577   Comprehensive Reference. New York: Academic Press. pp. 439–456. doi:10.1016/B978-
578   012370880-9.00278-4

579 Reese BE, Keeley PW. 2015. Design principles and developmental mechanisms underlying
580   retinal mosaics. *Biol Rev Camb Philos Soc* **90**:854–876. doi:10.1111/brv.12139

581 Reese BE, Necessary BD, Tam PP, Faulkner-Jones B, Tan SS. 1999. Clonal expansion and cell
582   dispersion in the developing mouse retina. *Eur J Neurosci* **11**:2965–2978.
583   doi:10.1046/j.1460-9568.1999.00712.x

584 Reitner A, Sharpe LT, Zrenner E. 1991. Is colour vision possible with only rods and blue-sensitive
585   cones? *Nature* **352**:798–800. doi:10.1038/352798a0

586   Rhim I, Coello-Reyes G, Ko H-K, Nauhaus I. 2017. Maps of cone opsin input to mouse V1 and
587   higher visual areas. *J Neurophysiol* **117**:1674–1682. doi:10.1152/jn.00849.2016
588   Rodieck RW. 1991. The density recovery profile: a method for the analysis of points in the plane
589   applicable to retinal studies. *Vis Neurosci* **6**:95–111. doi:10.1017/s095252380001049x
590   Röhlich P, van Veen T, Szél A. 1994. Two different visual pigments in one retinal cone cell.
591   *Neuron* **13**:1159–1166. doi:10.1016/0896-6273(94)90053-1
592   Schiviz AN, Ruf T, Kuebber-Heiss A, Schubert C, Ahnelt PK. 2008. Retinal cone topography of
593   artiodactyl mammals: influence of body height and habitat. *J Comp Neurol* **507**:1336–
594   1350. doi:10.1002/cne.21626
595   Schmidt BP, Boehm AE, Tuten WS, Roorda A. 2019. Spatial summation of individual cones in
596   human color vision. *PLoS ONE* **14**:e0211397. doi:10.1371/journal.pone.0211397
597   Shekhar K, Lapan SW, Whitney IE, Tran NM, Macosko EZ, Kowalczyk M, Adiconis X, Levin JZ,
598   Nemesh J, Goldman M, McCarroll SA, Cepko CL, Regev A, Sanes JR. 2016.
599   Comprehensive Classification of Retinal Bipolar Neurons by Single-Cell Transcriptomics.
600   *Cell* **166**:1308-1323.e30. doi:10.1016/j.cell.2016.07.054
601   Shinozaki A, Hosaka Y, Imagawa T, Uehara M. 2010. Topography of ganglion cells and
602   photoreceptors in the sheep retina. *J Comp Neurol* **518**:2305–2315.
603   doi:10.1002/cne.22333
604   Stabio ME, Sabbah S, Quattrochi LE, Ilardi MC, Fogerson PM, Leyrer ML, Kim MT, Kim I, Schiel M,
605   Renna JM, Briggman KL, Berson DM. 2018a. The M5 Cell: A Color-Opponent Intrinsically
606   Photosensitive Retinal Ganglion Cell. *Neuron* **97**:150-163.e4.
607   doi:10.1016/j.neuron.2017.11.030
608   Stabio ME, Sondereker KB, Haghgou SD, Day BL, Chidsey B, Sabbah S, Renna JM. 2018b. A novel
609   map of the mouse eye for orienting retinal topography in anatomical space. *J Comp
610   Neurol* **526**:1749–1759. doi:10.1002/cne.24446
611   Sterratt DC, Lyngholm D, Willshaw DJ, Thompson ID. 2013. Standard anatomical and visual
612   space for the mouse retina: computational reconstruction and transformation of
613   flattened retinae with the Retistruct package. *PLoS Comput Biol* **9**:e1002921.
614   doi:10.1371/journal.pcbi.1002921
615   Szatko KP, Korympidou MM, Ran Y, Berens P, Dalkara D, Schubert T, Euler T, Franke K. 2019.
616   Neural circuits in the mouse retina support color vision in the upper visual field. *bioRxiv*
617   745539. doi:10.1101/745539
618   Szél A, Diamantstein T, Röhlich P. 1988. Identification of the blue-sensitive cones in the
619   mammalian retina by anti-visual pigment antibody. *J Comp Neurol* **273**:593–602.
620   doi:10.1002/cne.902730413
621   Szél A, Lukáts A, Fekete T, Szepessy Z, Röhlich P. 2000. Photoreceptor distribution in the retinas
622   of subprimate mammals. *J Opt Soc Am A Opt Image Sci Vis* **17**:568–579.
623   doi:10.1364/josaa.17.000568
624   Szél A, Röhlich P, Caffé AR, Juliusson B, Aguirre G, Van Veen T. 1992. Unique topographic
625   separation of two spectral classes of cones in the mouse retina. *J Comp Neurol* **325**:327–
626   342. doi:10.1002/cne.903250302
627   Wang YV, Weick M, Demb JB. 2011. Spectral and temporal sensitivity of cone-mediated
628   responses in mouse retinal ganglion cells. *J Neurosci* **31**:7670–7681.
629   doi:10.1523/JNEUROSCI.0629-11.2011

630   Warwick RA, Kaushansky N, Sarid N, Golan A, Rivlin-Etzion M. 2018. Inhomogeneous Encoding
631   of the Visual Field in the Mouse Retina. *Curr Biol* **28**:655-665.e3.
632   doi:10.1016/j.cub.2018.01.016
633   Yang H, Wang H, Shivalila CS, Cheng AW, Shi L, Jaenisch R. 2013. One-step generation of mice
634   carrying reporter and conditional alleles by CRISPR/Cas-mediated genome engineering.
635   *Cell* **154**:1370–1379. doi:10.1016/j.cell.2013.08.022
636   Yilmaz M, Meister M. 2013. Rapid innate defensive responses of mice to looming visual stimuli.
637   *Curr Biol* **23**:2011–2015. doi:10.1016/j.cub.2013.08.015
638   Yokoyama S, Yokoyama R. 1989. Molecular evolution of human visual pigment genes. *Mol Biol*
639   *Evol* **6**:186–197. doi:10.1093/oxfordjournals.molbev.a040537
640   Zimmermann MJY, Nevala NE, Yoshimatsu T, Osorio D, Nilsson D-E, Berens P, Baden T. 2018.
641   Zebrafish Differentially Process Color across Visual Space to Match Natural Scenes. *Curr*
642   *Biol* **28**:2018-2032.e5. doi:10.1016/j.cub.2018.04.075
643

644 **8. METHODS**
645
646 **8.1. KEY RESOURCES**
647

Key Resources Table				
Reagent type (species) or resource	**Designation**	**Source or reference**	**Identifiers**	**Additional information**
strain, strain background (*Mus musculus*, male)	C57BL/6J mouse strain	Jackson Laboratory	Cat#000664, RRID:IMSR_JAX:000664	Pigmented mouse inbred strain
strain, strain background (*Mus musculus*, male)	Crl:CD-1(ICR) mouse strain	Charles River	Cat#022, RRID:IMSR_CRL:022	Albino mouse strain
strain, strain background (*Mus musculus*, male)	Copine9-Venus mouse line	This paper		Material and methods section 8.3.1
antibody	anti-OPN1SW (N-20) (Goat polyclonal)	Santa Cruz Biotechnology	Cat#sc-14363, RRID:AB_2158332	IF (1:1200)
antibody	anti-Opsin Red/Green (Rabbit polyclonal)	Millipore/Sigma	Cat#AB5405, RRID:AB_177456	IF (1:1000)
antibody	anti-Cone Arrestin (Rabbit polyclonal)	Millipore/Sigma	Cat#AB15282, RRID:AB_1163387	IF (1:300)
antibody	anti-GFP (Chicken polyclonal)	Millipore/Sigma	Cat#AB16901, RRID:AB_11212200	IF (1:100)

antibody	anti-Rabbit 488 (Donkey polyclonal)	Jackson Immunoresearch	Cat#711-547-003, RRID:AB_2340620	IF (1:500)
antibody	anti-Rabbit Cy3 (Donkey polyclonal)	Jackson Immunoresearch	Cat#711-165-152, RRID:AB_2307443	IF (1:500)
antibody	anti-Goat 647 (Donkey polyclonal)	Jackson Immunoresearch	Cat#705-605-147, RRID:AB_2340437	IF (1:500)
antibody	anti-Goat Cy3 (Donkey polyclonal)	Jackson Immunoresearch	Cat#705-166-147, RRID:AB_2340413	IF (1:500)
antibody	anti-Chicken 488 (Donkey polyclonal)	Jackson Immunoresearch	Cat#703-545-155, RRID:AB_2340375	IF (1:500)
sequence-based reagent	Copine9_gRNA_L(73/25)	This paper		5'GAGACATGACTGGTCCAA3'
sequence-based reagent	Copine9_gRNA_R(62/4.40),	This paper		5'GCCTCGGAGCGTAGCGTCC3'
software, algorithm	Zen	Zeiss	Zen lite Black edition 2.3 SP1	
software, algorithm	FIJI-ImageJ	NIH	v1.52r	https://imagej.nih.gov/ij/
software, algorithm	Sigma Plot	Systat Software	13.0	

software, algorithm	GraphPad Prism	Graph Pad Software	8.3.0	
software, algorithm	Photoshop	Adobe	CC 20.0.6	
software, algorithm	MATLAB	MathWorks	2016	
software, algorithm	R	The R Project for Statistical Computing	3.5.3	https://www.r-project.org/
software, algorithm	Retina and Visual Space Retistruct Package	Sterratt DC et al., PLoS Comput Biol.		
software, algorithm	Zotero	Corporation for Digital Scholarship	5.0	https://www.zotero.org/download/
other	DAPI	ThermoFisher Scientific	Cat# D3571, RRID:AB_2307445	(1ug/ml)

648

8.2. LEAD CONTACT AND MATERIALS AVAILABILITY

649
650 Further information and requests for resources and reagents should be directed to and will be
651 fulfilled by the Lead Contact, Wei Li (liwei2@nei.nih.gov).
652

8.3. METHOD DETAILS

653
654

8.3.1. Animal generation, handling and ethic statement

655
656 Three months old male pigmented (C57BL/6J, n=5), albino (CD1, n=5) mice were obtained from
657 the National Eye Institute breeding colony. The Venus-Cpne9 mouse line (n=5; based on
658 previous single cell sequencing data (Shekhar et al., 2016)) carries a reporter (Venus) allele
659 under the control of the mouse Cpne9 locus. The reporter allele was created directly in
660 B6.SJL(F1) zygotes using CRISPR-mediated homologous recombination (HR) (Yang et al., 2013).
661 Briefly, a HR targeting template was assembled with PCR fragments of 5' and 3' homology arms
662 of 910 bp and 969 bp respectively, flanking exon one, and a Venus expression cassette carrying
663 the bovine growth hormone polyadenylation (bGH-PolyA) signal sequence as the terminator.
664 Homology arms were designed such that integration of the reporter cassette would be at the

665 position right after the first codon of the Cpne9 gene in exon one. A pair of guide RNAs (gRNA),
666 with outward orientation (38 bp apart), were synthesized by *in vitro* transcription as described
667 (Yang et al., 2013) and tested for their efficiency and potential toxicity in a zygote
668 differentiation assay where mouse fertilized eggs were electroporated with SpCas9 protein and
669 gRNA ribonuclear particles. Eggs were cultured in vitro for 4 days in KSOM (Origio Inc, CT) until
670 differentiated to blastocysts. Viability and indel formation were counted respectively. gRNA
671 sequences are (1) Copine9_gRNA_L(73/25), 5'GAGACATGACTGGTCCAA3'; (2)
672 Copine9_gRNA_R(62/4.40), 5'GCCTCGGAGCGTAGCGTCC3'. A mixture of the targeting plasmid
673 (super coiled, 25ng/μl) with two tested gRNAs (25 ng/μl each) and the SpCas9 protein (Life
674 Science technology, 30ng/μl) were microinjected into mouse fertilized eggs and transferred to
675 pseudopregnant female recipients as described elsewhere (Yang et al., 2013). With a total of 15
676 F0 live births from 6 pseudopregnant females, 11 were found to carry the knockin allele by
677 homologous recombination, a HR rate of 73%. F0 founders in B6.SJL F1 (50% C57BL6 genome)
678 were crossed consecutively for 3 generations with C57BL6/J mice to reach near congenic state
679 to C57BL6/J.
680 Mice were housed a 12:12 hours light/dark cycle. All experiments and animal care are
681 conducted in accordance with protocols approved by the Animal Care and Use Committee of
682 the National Institutes of Health and following the Association for Research in Vision and
683 Ophthalmology guidelines for the use of animals in research.
684
685 **8.3.2. Tissue collection**
686 All animals were sacrificed with an overdose of CO_2 and perfused transcardially with saline
687 followed by 4% paraformaldehyde. To preserve retinal orientation, eight retinas per mouse
688 strain/line were dissected as flat whole-mounts by making four radial cuts (the deepest one in
689 the dorsal pole previously marked with a burn signal as described (Nadal-Nicolás et al., 2018;
690 Stabio et al., 2018b). The two remaining retinas were cut in dorso-ventral orientation (14μm)
691 after cryoprotection in increasing gradients of sucrose (Sigma-Aldrich SL) and embedding in
692 optimal cutting temperature (OCT; Sakura Finetek).
693
694 **8.3.3. Immunohistochemical labeling**
695 Immunodetection of flat-mounted retinas or retinal sections was carried out as previously
696 described (Nadal-Nicolás et al., 2018). Importantly, the retinal pigmented epithelium was
697 removed before the immunodetection. First, whole-retinas were permeated (4x10') in PBS 0.5%
698 Triton X-100 (Tx) and incubated by shaking overnight at room temperature with S-opsin (1:1200)
699 and M-opsin (1:1000) or cone arrestin (1:300) primary antibodies diluted in blocking buffer (2%
700 normal donkey serum). Cpne9-Venus retinas were additionally incubated with an anti-GFP
701 antibody (1:100) to enhance the original Venus signal. Retinas were washed in PBS 0.5% Tx
702 before incubating the appropriate secondary antibodies overnight (1:500). Finally, retinas were
703 thoroughly washed prior to mounting with photoreceptor side up on slides and covered with
704 anti-fading solution. Retinal sections were counterstained with DAPI.
705
706 **8.3.4. Image acquisition**
707 Retinal whole-mounts were imaged with a 20x objective using a LSM 780 Zeiss confocal
708 microscope equipped with computer-driven motorized stage controlled by Zen Lite software

709　(Black edition, Zeiss). M- and S-opsins were imaged together to allow the identification and
710　quantification of different cone types. Magnifications from flat mounts and retinal cross-
711　sections (Figure 1) were taken from dorsal, medial and ventral areas using a 63x objective for
712　opsin co-expression analysis. Images from retinal cross-sections were acquired ~1.5mm dorsally
713　or ventrally from the optic disc.

714

715　**8.3.5. Sampling and opsin co-expression measurement**
716　In four retinas per strain, we acquired images from three 135x135 μm samples (63x) per each
717　area of interest (dorsal, medial and ventral). These areas were selected according to the S-opsin
718　gradient in wholemount retinas (see scheme in Figure 1C). Cone outer segments were manually
719　classified as M^+S^-, true S- (S^+M^-) or mixed (M^+S^+) cones depending on their opsin expression.
720　Data representation was performed using GraphPad Prism 8.3 software.

721

722　**8.3.6. Image processing: manual and automated whole quantification**
723　To characterize the distribution of the different cone photoreceptor types in the mouse retina,
724　we developed and validated an automatic routine (ImageJ, NIH) to identify, quantify the total
725　number of outer segments and finally extract the location of each individual cone (Figure 2-
726　figure supplement 1A). Briefly, maximum-projection images were background-subtracted and
727　thresholded (background-noise mean value, 9.6±1.2% and 15.2±3.2% for S- and M-opsin
728　respectively, the threshold was applied at 15.7%) to create a binary mask that was then
729　processed using watershed and despeckle filters to isolate individual cones and reduce noise.
730　The "3D Objects Counter" plugin was applied to such images to count cones within fixed
731　parameters (shape and size) and extract their *xy* coordinates for further analysis. This
732　automation was validated by statistical comparison with manual counting performed by an
733　experienced investigator (Pearson correlation coefficient R^2 = 96-99% for M- or S-opsin
734　respectively, Figure 2-figure supplement 1B). To count cone subtypes, images were pre-
735　processed with image processing software (Adobe Photoshop CC) to isolate the desired subtype
736　and then manually marked using Photoshop, or automatically counted using ImageJ as
737　described above. Total cone populations were determined by combining M- and S-opsin
738　channels, while mixed M^+S^+ cones were obtained by masking the M-opsin signal with the S-
739　opsin channel. M^+S^- cones in pigmented mice were obtained by subtracting the S-opsin signal
740　from the M-opsin photomontage. Finally, M^+S^- cones (in albino samples), true S-cones (both
741　strains) (Figure 2-figure supplement 1C) and Venus$^+$ SCBCs (Cpne9-Venus mouse line) were
742　manually marked on the retinal photomontage (Adobe Photoshop CC).

743

744　**8.3.7. Topographical distributions.**
745　Topographical distributions of cone population densities were calculated from cone locations
746　identified in whole-mount retinas using image processing (see above). From these populations,
747　isodensity maps were created using Sigmaplot 13.0 (Systat Software). These maps are filled
748　contour plots generated by assigning to each area of interest (83.3x83.3 μm) a color code
749　according to its cone density, ranging from 0 (purple) to 17,300 cones/mm^2 for all cone types
750　except for true S-cones and M^+S^--cone in the albino strain (5,000 cones/mm^2), as represented in
751　the last image of each row of Figure 2A, or 1,400 SCBCs/mm^2 (Figure 3D) within a 10-step color-
752　scale. These calculations allow as well, the illustration of the number of cones at a given

753 position from the ON center. To analyze the relative opsin expression along the retinal surface,
754 we have considered three cone populations (mixed, M$^+$S$^-$ and true S-cones) dividing the retina
755 in four quadrants: dorsotemporal, dorsonasal, ventrotemporal and ventronasal (DT, DN, VT and
756 VN respectively, scheme in Figure 2C). The relative percentage of cone-types are represented in
757 line graphs from four retinas/strain (SigmaPlot 13.0).

758

759 **8.3.8. SCBC sampling and 'true S-cone' connectivity**
760 To characterize the connectivity of Venus$^+$ S-cone bipolar cells (Venus$^+$ SCBCs) with true S-cone
761 terminals, we acquired images from the same area (260x260 µm, 63x) at two focal planes: First,
762 we focused upon the INL+OPL, then the corresponding photoreceptor outer segment (OS) layer,
763 respectively, for two areas of interest (DT and VN). To verify connectivity between Venus$^+$ SCBC
764 dendrites and true S-cone pedicles in the OPL, in addition to S-opsin immunodetection, we also
765 labeled retinas using cone arrestin antibodies to discriminate mixed cone pedicles from true S-
766 cone pedicles, because true S-cone pedicles contain either low or no cone arrestin (Figure 3B,
767 Haverkamp et al., 2005). In other retinas, SCBC contacts were verified by tracking each cell body
768 from cone pedicles to their respective OS to confirm S$^+$M$^-$ opsin labeling (Figure 3C). In five
769 retinas (with S- and M-opsin double immunodetection), we analyzed the connectivity between
770 186 Venus$^+$ SCBCs (133 and 53 for DT and VN respectively) and 263 true S-cone pedicles (74 and
771 189, DT and VN respectively). The number of synaptic contacts was assessed by tracking
772 manually each SCBC-branch from the cell body using the Zen lite black visualization package (Z-
773 stack with 1µm interval). Multiple branch contacts in one true S-cone pedicle from a single
774 SCBC were considered a single contact and counted only once (Figure 3B), while secondary
775 bifurcations were considered as multiple contacts (Figure 3c'). SCBC-blind endings were not
776 counted (Figure 3c"). The average number of contacts per retina was used to calculate the DT
777 and VN means (Supplementary file 2 and graphs in 3C).

778

779 **8.3.9. Clustering analysis. K-neighbor maps and variance analysis of Voronoi dispersion.**
780 To assess the true S-cones and S-cone bipolar cell (SCBC) clustering, we performed two
781 comparable sets of analyses. First, we extracted two circular areas (1mm diameter) in the DT-
782 VN axis at 1mm from the optic disc center (scheme in 4B). A K-nearest neighbor algorithm
783 (Nadal-Nicolás et al., 2014) was used to map the number of neighboring true S-cones within a
784 18 µm radius of each true S-cone to a color-code in its retinal position (Figure 4B). Regularity
785 indices were computed for each retinal sample using Voronoi diagrams for cone positions as
786 well as nearest neighbor distances (VDRI and NNRI, respectively (Reese and Keeley, 2015);
787 Figure 4C-E). NNRIs were computed as the ratio of the mean to the standard deviation for the
788 distance from true S-cones to their nearest true S-cone neighbor. true S-cone neighbor ratios
789 (SCNR) were calculated for each retinal sample as the average proportion of true s-cones within
790 a given radius for each cone. This search radius was calculated separately for each sample to
791 correct for sample-to-sample variations in total density: this radius (r) was calculated as $r = 3\sqrt{}$
792 ($A / (\sqrt{2}\,\pi N)$), where A is the circular area of the 1mm diameter retinal sample and N is the total
793 number of cones in that sample. For a highly regular cell mosaic containing N cells filling an area
794 A, this calculation estimates the location of the first minimum in the density recovery profile
795 (Rodieck, 1991), providing the average radius of a circle centered upon a cone that will

796   encompass its first tier of cone neighbors (but exclude the second tier) in an evenly distributed
797   mosaic. To minimize edge effects from computations of NNRI, VDRI, SCNR, those values for
798   cones closer to the outer edge of the sample than the SCNR search radius were discarded. To
799   produce simulated cone mosaics for comparison with observed values, cone distributions with
800   evenly "distributed" true S-cones were generated by first using a simple mutual repulsion
801   simulation to maximize the distances between true S-cones, followed by assigning the nearest
802   positions among all cone locations as being "true S". "Shuffled" populations of true S-cones
803   were generated by permuting cone identities randomly among all cone locations, holding the
804   proportion of true S-cones constant. Voronoi diagrams, neighbor calculations, and mosaic
805   generation and other computations were performed using MATLAB R2016b.
806
807   **8.3.10. True S-cone cluster and SCBC synaptic contacts evaluation**
808   To characterize the true S-cone cluster connectivity in the VN retina, retinal whole-mounts
809   were imaged with a 63x objective, from the photoreceptor outer segments to the OPL, in a Z-
810   stack image with 0.5μm interval. To visualize the true S-cone clustering and Venus$^+$ SCBC
811   connectivity, we identified numerically, and color coded each true S-outer segment form a
812   cluster. The corresponding true S-pedicles were identified by tracking the cell body from their
813   S$^+$M$^-$OSs. Focusing on the outer plexiform layer (OPL), each individual true S-cone pedicle -that
814   form a cluster- was manually outlined and color coded accordingly. Lastly, the SCBC synaptic
815   terminals, that belong to a single SCBC, were identified by their specific contacts to the
816   respective true S-cone pedicle (Figure 4F).
817
818   **8.3.11. Retinal reconstruction and visuotopic projection**
819   Retinal images were reconstructed and projected into visual space using R software v.3.5.2 for
820   64-bit Microsoft Windows using Retistruct v.0.6.2 as in Sterratt et al. (2013). Reconstruction
821   parameters from that study were used: namely, a rim angle of 112° (phi$_0$ = 22°), and eye
822   orientation angles of 22° (elevation) and 64° (azimuthal). For figure 4-figure supplement 1, true
823   S-cone density contour lines and heatmaps were computed in MATLAB and overlaid onto flat-
824   mount retina opsin labeling images using ImageJ prior to processing by Retistruct.
825
826   **8.3.12. Statistical analysis**
827   Statistical comparisons for the percentage of cones/retinal location, the total cone
828   quantifications (Supplementary file 1) and the DT or VN true S-cones and Venus$^+$SCBCs
829   (Supplementary file 2) were carried out using GraphPad Prism v8.3 for Microsoft Windows.
830   Data are presented as mean ± standard deviation. All data sets passed the D'Agostino-Pearson
831   test for normality, and the comparisons between strains were performed with Student's *t*-test.
832
833   For each 1mm retinal sample, VDRI, NNRI, and SCNR values were normalized and compared to
834   the distributions of "shuffled" cone populations. Such comparisons were not performed against
835   "distributed" populations, because in those populations, VDRI and NNRI values were
836   consistently much higher—and SCNR much lower—than in real samples (see Figure 4D-E). The
837   "shuffled" populations for each retinal region produced measurements that were well
838   described by normal distributions (Kolmogorov-Smirnov test, MATLAB). Thus, to allow
839   comparisons across samples, we converted each measurement into a *Z*-score using the mean

840   and standard deviation of those measures from shuffled populations. One-tailed Student's *t*-
841   tests were performed to compare the normalized measures to the distribution of "randomly
842   shuffled" cone population measures, and significance was determined at the $p<0.05$ level.
843
844   **9. SUPPLEMENTARY MATERIAL**
845
846   **Supplementary file 1.** (A) Cone numbers in different retinal areas along the dorsoventral axis in
847   pigmented and albino mouse. Three images/area (dorsal, medial and ventral) from four
848   retinas/strain. Different cone type quantifications are shown as average ± SD, corresponding to
849   the percentages shown in Fig 1C. The total number of cones analyzed per location and strain
850   are shown in the last column. Total number of cones (B) or S-cone Bipolar cells (SCBCs, C) in
851   eight retinas/mouse strain or line (average ± SD, see also Figure 2B). Significant differences
852   between strains $p<0.05$ (*), $p<0.01$ (**), $p<0.001$ (***), $p<0.0001$ (****).
853
854   **Supplementary file 2.** True S-cone terminals and Cpne9-Venus+SCBCs connectivity in
855   dorsotemporal (DT) and ventronasal retina (VN). Quantitative data are shown as mean ± SD
856   from the average of five DT and VN retinal areas (Figure 3C). Significant differences between
857   retinal areas, $p<0.01$ (**), $p<0.0001$ (****).
858
859   **Supplementary file 3.** Numbers of true S-cones (A) and Cpne9-Venus[+]SCBCs (B) in
860   dorsotemporal (DT) and ventronasal (VN) circular areas (1mm diameter, Figs 3E and 4B).
861   Quantitative data are shown as average ± SD from eight retinas/strain or line. The mean of true
862   S-cones and Venus[+]SCBCs in these circular areas was used to calculate the DT:VN and true S-
863   cone:SCBC (C) ratios. Significant differences between strains $p<0.05$ (*), $p<0.001$ (***). True S-
864   cones and SCBCs were significant different between DT and VN retina ($p<0.0001$).